

# Communication

## 2-D Electromagnetic Scattering From Multiple Arbitrarily Anisotropic Inhomogeneities Embedded in Multilayered Biaxially Anisotropic Elliptical Cylinders Solved by the Hybrid SIM/SEM

Zhen Guan<sup>ID</sup>, Jiawen Li<sup>ID</sup>, and Feng Han<sup>ID</sup>

**Abstract**—In this communication, the 2-D electromagnetic (EM) scattering from multiple inhomogeneous arbitrarily anisotropic scatterers embedded inside multilayered biaxially anisotropic elliptical cylinders when the illumination source is transverse electric ( $TE_z$ ) polarized is formulated and solved by the hybrid spectral integral method (SIM) and spectral element method (SEM). The multiple smooth elliptical boundaries are discretized in the framework of 1-D integral equations (IEs), and the equivalent current on the boundaries is solved for by SIM. In contrast, the multiple inhomogeneous regions containing the anisotropic scatterers are separately discretized in the framework of 2-D Helmholtz equations and the magnetic fields inside the regions are solved by SEM with the 1-D boundary integration to truncate the computational domain. The multilayered SIM system matrix and the multiple SEM system matrices are coupled together by the radiation boundary conditions to form the final system matrix. Based on this matrix, both the equivalent current in multiple boundaries and the magnetic fields inside multiple inhomogeneous scatterers are simultaneously solved. Two numerical experiments are carried out to validate the computation precision and efficiency of the proposed hybrid method.

**Index Terms**—Anisotropy, electromagnetic (EM) scattering, multilayered elliptical cylinders, spectral element method (SEM), spectral integral method (SIM).

### I. INTRODUCTION

Electromagnetic (EM) scattering refers to the physical process in which the incident wave interacts with specific targets, and thus the wave parameters such as the amplitude and phase are changed. Its wide applications include microwave imaging [1], subsurface detection [2], geophysical exploration [3], artificial material design [4], and so on.

One of the commonly used methods to solve EM scattering problems is to formulate them using the integral equation (IE) which includes both the unknown total fields and the integral of the multiplication of the unknown total fields and Green's functions. Therefore, the IE usually has no analytical solution and it can be discretized and numerically solved by the method of moment (MoM) [5]. Unfortunately, the computational cost of the traditional MoM is unaffordable [6]. Several improved numerical methods have been

proposed in the past decades. They mainly include the conjugate gradient method [7], the adaptive integral method [8], the fast multipole algorithm [9], the precorrected fast Fourier transform (FFT) [10], the stabilized biconjugate gradient accelerated by FFT [11], etc. In these IE-based methods, the computational domain is usually restricted in a limited region that can tightly wrap the scatterers, and the transceivers are allowed to be placed far from the domain. However, because they are highly dependent on Green's functions, their applications to the scattering problems with irregular background media are problematical since Green's functions are usually not easy to evaluate for arbitrarily irregular media.

The differential equation (DE) can adapt to arbitrarily inhomogeneous background media since it directly describes the local EM fields which also can be directly solved for as long as some proper boundary conditions are imposed. Usually, the differential-form Maxwell equations or the Helmholtz equations are discretized and numerically solved. The commonly used DE-based numerical approaches include the finite-difference frequency-domain (FDFD) method [12], the finite-difference time-domain (FDTD) method [13], the finite element method (FEM) [14], the spectral element method (SEM) [15], etc. The drawback of these DE-based methods is that the computational domain always encloses the transceivers when the absorbing boundary conditions are imposed, which inevitably leads to high costs when transceivers are far from the scatterers.

In this communication, we hybridize the IE-based method and the DE-based method to efficiently solve the 2-D EM scattering from multiple inhomogeneous scatterers embedded inside multiple elliptical cylinders. Specifically speaking, we formulate the EM scattering from the multilayered biaxially anisotropic elliptical cylinders using 1-D surface IEs but formulate the EM scattering from the multiple arbitrarily anisotropic inhomogeneous scatterers embedded inside the cylindrical layers using 2-D Helmholtz equations. Meanwhile, to enhance the implementation efficiency, the 1-D surface IEs are discretized and solved using the spectral integral method (SIM) [16] instead of using the traditional MoM while the 2-D Helmholtz equations are discretized and solved using SEM [17] instead of using the traditional FEM. The system matrix of the multilayered SIM and the system matrices for multiple SEM regions are coupled together to form the final spectral-element spectral-integral (SESI) system matrix via multiple radiation boundary conditions which are also formulated in the spectral domain in this work. Although there are also other hybrid methods proposed in previous works, e.g., [18] and [19] dealing with the similar scattering problem, most of them adopt the traditional FEM and MoM to solve EM scattering from 2-D objects wrapped in an isolated domain. In [20], although SIM is used, it is hybridized with FEM to compute EM fields scattered from an isolated scatterer buried in a layered medium. This work is the extension of our previous works [17] and [21] and its major new contribution is that the EM scattering from multiple inhomogeneous arbitrarily

Manuscript received 5 February 2024; revised 3 June 2024; accepted 25 June 2024. This work was supported by the National Natural Science Foundation of China under Grant 62271428. (Corresponding author: Feng Han.)

Zhen Guan is with the School of Science, Tianjin University of Technology, Tianjin 300384, China (e-mail: zguan@email.tjut.edu.cn).

Jiawen Li is with the School of Electronic and Information Engineering, Guangxi Normal University, Guilin, Guangxi 541004, China (e-mail: jiawenli@mailbox.gxnu.edu.cn).

Feng Han is with the School of Computing and Information Technology, Great Bay University, Dongguan, Guangdong 523000, China, and also with the Institute of Electromagnetics and Acoustics, Xiamen University, Xiamen 361005, China (e-mail: feng.han@gbu.edu.cn).

Color versions of one or more figures in this article are available at <https://doi.org/10.1109/TAP.2024.3420431>.

Digital Object Identifier 10.1109/TAP.2024.3420431

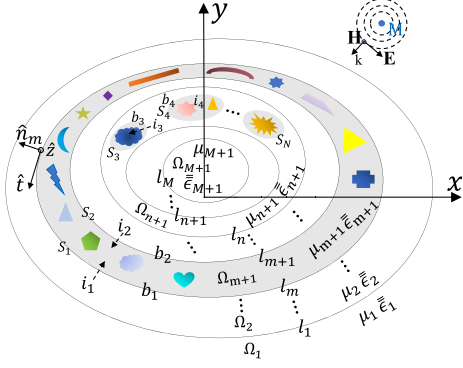


Fig. 1. Multiple 2-D inhomogeneous scatterers embedded inside multilayered nonconcentric elliptical cylinders illuminated by an EM wave that is excited by a magnetic dipole source  $\mathbf{M}$ .

anisotropic scatterers embedded in multiple 2-D biaxially anisotropic elliptical cylinders is computed by the hybrid SESI method. It is also different from [22] since we consider the anisotropy in this work. In addition, SIM is only hybridized with SEM implemented in a whole circular ring in [22]. In contrast, in our current work, SIM is also hybridized with SEM implemented in several isolated domains embedded inside an elliptical ring, which significantly increase the system matrix complexity due to the mutual coupling between those isolated domains and the elliptical boundaries. Although the proposed hybrid SESI method has the limitation that the boundaries of both the multilayered background medium and those embedded isolated regions must be smooth ellipses to allow the EM field expansion with low-order Fourier series [21], it still has the potential applications in fast microwave imaging of multiple scatterers embedded inside cylindrically shaped objects [23], design of microstrip antennas mounted on multilayered circular cylinders [24], EM induction and dielectric logging [25], etc.

The rest of this communication is organized as follows. In Section II, the 2-D SESI formulas for EM scattering by multiple inhomogeneous scatterers embedded inside multiple elliptical cylinders are derived based on the previous formulas given in [17] and [21]. In Section III, two numerical examples are presented to validate the correctness and computation efficiency of the derived formulas. In Section IV, the conclusion and discussion are presented.

## II. METHODS

As shown in Fig. 1, the background medium includes  $M$  elliptical cylindrical boundaries which are denoted as  $l_1, \dots, l_M$ . The elliptical regions  $\Omega_1, \dots, \Omega_{M+1}$  are biaxially anisotropic. They are illuminated by an EM wave that is excited by a magnetic dipole source  $\mathbf{M}$  and has the transverse electric (TE<sub>z</sub>) polarization. These basic configurations are the same as those shown in [21, Fig. 1]. Therefore, we still formulate the magnetic fields on the boundaries  $l_1, \dots, l_M$  using 1-D surface IEs and solve them using SIM. On the other hand, we place several arbitrarily anisotropic inhomogeneous scatterers in the region  $\Omega_{m+1}$  which is enclosed by the  $l_m$ th and  $l_{m+1}$ th boundaries and in the region  $\Omega_{n+1}$  which is enclosed by the  $l_n$ th and  $l_{n+1}$ th boundaries. Because the scatterers placed inside the region  $\Omega_{m+1}$  are dense, the whole region is directly discretized and the EM fields inside it are solved by SEM. In contrast, those isolated scatterers placed inside the region  $\Omega_{n+1}$  are sparse. So we enclose them with the smooth elliptical surfaces  $S_3, \dots, S_M$ , discretize these isolated domains, and solve the EM fields inside them with the hybrid SESI method [17]. To derive the mathematical formulas for this complex EM scattering model, we first return back to the simple model when those inhomogeneous scatterers are absent and rewrite

the system matrix equation according to [21, eq. (23)] as

$$\mathbf{Z}\mathbf{I} = \mathbf{V} \quad (1)$$

where  $\mathbf{Z}$  is a block-by-block tridiagonal matrix and has the dimensions of  $2\Sigma_{k=1}^M N_k \times 2\Sigma_{k=1}^M N_k$  in which  $N_k$  is the number of the discrete points of SIM on the  $k$ th smooth elliptical boundary  $l_k$ . In addition, one should note that the system matrix  $\mathbf{Z}$  is actually cascaded by a series of submatrices that represent either the self-coupling or the mutual coupling of EM fields and equivalent current on elliptical boundaries, according to the surface equivalence theorem. The self-coupling refers to the situation that the equivalent current and the EM field observation points are located on the same boundary. In contrast, the mutual coupling refers to the situation that the EM field observation points are located on two adjacent boundaries to that on which the equivalent current is located. See [21, eqs. (2) and (3)]. Let us take the region  $\Omega_{m+1}$  as an example and pick the submatrix between the rows of  $2\Sigma_{k=1}^{m-1} N_k + N_m + 1$  and  $2\Sigma_{k=1}^m N_k + N_{m+1}$  and between the columns of  $2\Sigma_{k=1}^{m-1} N_k + 1$  and  $2\Sigma_{k=1}^m N_k$  of  $\mathbf{Z}$ . It is written as

$$\mathbf{Z}_{\Omega_{m+1}} = \begin{bmatrix} \mathbf{Z}_{J,m,m}^{\text{in}} & \mathbf{Z}_{M,m,m}^{\text{in}} & \mathbf{Z}_{J,m,m+1} & \mathbf{Z}_{M,m,m+1} \\ \mathbf{Z}_{J,m+1,m} & \mathbf{Z}_{M,m+1,m} & \mathbf{Z}_{J,m+1,m+1}^{\text{out}} & \mathbf{Z}_{M,m+1,m+1}^{\text{out}} \end{bmatrix} \quad (2)$$

which has the dimensions of  $\Sigma_{k=m}^{m+1} N_k \times 2\Sigma_{k=m}^{m+1} N_k$ . The superscript “out” means both the equivalent source point and the field point are located on the outer side of a certain elliptical boundary while “in” means they are located on the inner side. The three characters of the subscript denote the source type, field-point boundary, and source-point boundary, respectively. For example, the subscript of  $\mathbf{Z}_{M,m,m+1}$  means the field point is located on the  $l_m$ th boundary and the equivalent magnetic source is located on the  $l_{m+1}$ th boundary. The unknown vector  $\mathbf{I}$  is composed of the Fourier spectral coefficients of the magnetic fields and tangential electric fields in all  $M$  elliptical boundaries and is constructed as

$$\mathbf{I} = \begin{bmatrix} \tilde{\mathbf{H}}_{z,1}^T & \tilde{\mathbf{E}}_{t,1}^T & \cdots & \tilde{\mathbf{H}}_{z,m}^T & \tilde{\mathbf{E}}_{t,m}^T & \cdots & \tilde{\mathbf{H}}_{z,M}^T & \tilde{\mathbf{E}}_{t,M}^T \end{bmatrix}^T \quad (3)$$

which has the dimensions of  $2\Sigma_{k=1}^M N_k \times 1$ . The vector  $\mathbf{V}$  in (1) is composed of the incident magnetic fields in the outermost elliptical boundary and written as

$$\mathbf{V} = \begin{bmatrix} (\mathbf{H}_{z,1}^{\text{inc}})^T & \mathbf{0} & \cdots & \mathbf{0} \end{bmatrix}^T \quad (4)$$

which also has the dimensions of  $2\Sigma_{k=1}^M N_k \times 1$ . We now place multiple inhomogeneous scatterers in the region  $\Omega_{m+1}$ , discretize the whole ring between the  $l_m$ th and  $l_{m+1}$ th boundaries, and formulate it using the SESI method given [17]. In this situation, the self-coupling and mutual EM coupling on or between the  $l_m$ th and  $l_{m+1}$ th boundaries cannot be formulated by the SIM submatrices given in (2). Instead, they are formulated by the SEM submatrices. Therefore, we replace  $\mathbf{Z}_{\Omega_{m+1}}$  in (2) with a new SEM submatrix

$$\mathbf{Z}_{\Omega_{m+1}}^1 = \begin{bmatrix} \mathbf{Z}_{b_1,b_1}^1 \mathbf{T}_1 & \mathbf{Z}_{S_1} \mathbf{T}_1 & \mathbf{Z}_{b_1,i_1} & & \\ \mathbf{Z}_{i_1,b_1}^1 \mathbf{T}_1 & & \mathbf{Z}_{i_1,i_2} & \mathbf{Z}_{i_2,b_2}^1 \mathbf{T}_2 & \\ & \mathbf{Z}_{b_2,i_2} & \mathbf{Z}_{b_2,b_2}^1 \mathbf{T}_2 & \mathbf{Z}_{S_2} \mathbf{T}_2 & \end{bmatrix} \quad (5)$$

which is assembled similar to [17, eq. (13a)] but with the SEM region  $\Omega_{m+1}$  enclosed by both the  $l_m$ th (denoted by  $b_1$ ) and  $l_{m+1}$ th (denoted by  $b_2$ ) elliptical boundaries. In addition, both the superscripts  $i_1$  and

$i_2$  denote the region  $\Omega_{m+1}$ .  $\mathbf{T}_1$  and  $\mathbf{T}_2$  are the inverse Fourier transform matrices for the boundaries  $l_m$  and  $l_{m+1}$ , respectively. The definitions of  $\mathbf{T}$  and the submatrix  $\mathbf{Z}$  in (5) have been given in [17] and will not be repeated here. Note  $\mathbf{Z}_{\Omega_{m+1}}^1$  in (5) has the dimensions of  $(N_{b_1} + N_{i_1} + N_{b_2}) \times (2\sum_{k=m}^{m+1} N_k + N_{i_1})$  where  $N_{b_1}$ ,  $N_{b_2}$ , and  $N_{i_1}$  denote the numbers of discrete points of SEM on the  $l_m$ th boundary, on the  $l_{m+1}$ th boundary, and inside the region  $\Omega_{m+1}$ , respectively. Obviously, replacing  $\mathbf{Z}_{\Omega_{m+1}}$  in (2) with  $\mathbf{Z}_{\Omega_{m+1}}^1$  in (5) naturally increases the dimensions of the original system matrix  $\mathbf{Z}$  in (1) to  $(2\sum_{k=1}^M N_k + N_{b_1} + N_{i_1} + N_{b_2} - N_m - N_{m+1}) \times (2\sum_{k=1}^M N_k + N_{i_1})$  to form the new system matrix  $\mathbf{Z}^1$ . Therefore, we also increase the row number of the vector  $\mathbf{I}$  in (3) from  $2\sum_{k=1}^M N_k$  to  $2\sum_{k=1}^M N_k + N_{i_1}$ , insert the coefficient vector  $\mathbf{H}^{i_1}$  of the SEM nodes inside the region  $\Omega_{m+1}$  into  $\mathbf{I}$ , and form the new coefficient vector

$$\mathbf{I}^1 = \left[ \cdots \tilde{\mathbf{H}}_{Z,m}^T \quad \tilde{\mathbf{E}}_{t,m}^T \quad (\mathbf{H}^{i_1})^T \quad \tilde{\mathbf{H}}_{Z,m+1}^T \quad \tilde{\mathbf{E}}_{t,m+1}^T \cdots \right]^T. \quad (6)$$

We now further increase the complexity of the scattering model and add a series of isolated inhomogeneous scatterers in the region  $\Omega_{n+1}$ , as shown in Fig. 1. These scatterers are wrapped by the elliptical smooth boundaries  $S_3, S_4, \dots, S_N$ , respectively. Note the submatrix  $\mathbf{Z}_{\Omega_{n+1}}$  for the region  $\Omega_{n+1}$  is similar to  $\Omega_{m+1}$  in (2) but with  $m$  replaced with  $n$  when the isolated inhomogeneous scatterers are absent. However, when they are present, additional submatrices must be added to  $\mathbf{Z}_{\Omega_{n+1}}$  to account for the mutual EM coupling between the  $l_n$ th and  $l_{n+1}$ th boundaries and  $S_3, \dots, S_N$  and the mutual EM coupling among  $S_3, \dots, S_N$  themselves. In the following, we just take the scatterer wrapped by  $S_3$  as an example and discuss how it will enlarge the submatrix  $\mathbf{Z}_{\Omega_{n+1}}$ . We first construct the SESI submatrix for the inhomogeneous scatterer wrapped by  $S_3$  which is similar to [17, eq. (13a)] and it is written as

$$\mathbf{Z}_{\Omega_{S_3}} = \begin{bmatrix} \mathbf{Z}_{J,b_3,b_3}^{out} & \mathbf{Z}_{M,b_3,b_3}^{out} & \mathbf{0} \\ \mathbf{Z}_{b_3,b_3}^{\mathbf{T}_3} & \mathbf{Z}_{S_3}^{\mathbf{T}_3} & \mathbf{Z}_{b_3,i_3} \\ \mathbf{Z}_{i_3,b_3}^{\mathbf{T}_3} & \mathbf{0} & \mathbf{Z}_{i_3,i_3} \end{bmatrix} \quad (7)$$

where  $b_3$  refers to the boundary  $S_3$  while  $i_3$  refers to the inner region of  $S_3$ .  $\mathbf{T}_3$  is the inverse Fourier transform matrix for the boundary  $S_3$ . The definitions of the submatrices of (7) can be referred to [17, eq. (13a)]. Note that the dimensions of  $\mathbf{Z}_{\Omega_{S_3}}$  are  $(N_{S_3} + N_{b_3} + N_{i_3}) \times (2N_{S_3} + N_{i_3})$  where  $N_{i_3}$  and  $N_{b_3}$  denote the numbers of discrete points of SEM inside  $S_3$  and on  $S_3$ , respectively, while  $N_{S_3}$  denotes the number of discrete points of SIM on  $S_3$ . Then, we enlarge the dimensions of the matrix  $\mathbf{Z}_{\Omega_{n+1}}$  from  $(\sum_{k=n}^{n+1} N_k) \times (2\sum_{k=n}^{n+1} N_k)$  to  $(\sum_{k=n}^{n+1} N_k + N_{S_3} + N_{b_3} + N_{i_3}) \times (2\sum_{k=n}^{n+1} N_k + 2N_{S_3} + N_{i_3})$  and insert the  $\mathbf{Z}_{\Omega_{S_3}}$  into the center of the original matrix  $\mathbf{Z}_{\Omega_{n+1}}$ , that is, between the first  $N_n$  rows and the last  $N_{n+1}$  rows and between the first  $2N_n$  columns and the last  $2N_{n+1}$  columns. Now, let us consider the mutual EM coupling between  $S_3$  and the  $l_n$ th and  $l_{n+1}$ th boundaries. The corresponding matrices are constructed as  $\mathbf{Z}_{b_3,n} = [\mathbf{Z}_{J,b_3,n} \quad \mathbf{Z}_{M,b_3,n}] \in \mathbb{C}^{N_{S_3} \times 2N_n}$ ,  $\mathbf{Z}_{b_3,n+1} = [\mathbf{Z}_{J,b_3,n+1} \quad \mathbf{Z}_{M,b_3,n+1}] \in \mathbb{C}^{N_{S_3} \times 2N_{n+1}}$ ,  $\mathbf{Z}_{n,b_3} = [\mathbf{Z}_{J,n,b_3} \quad \mathbf{Z}_{M,n,b_3}] \in \mathbb{C}^{N_n \times 2N_{S_3}}$ , and  $\mathbf{Z}_{n+1,b_3} = [\mathbf{Z}_{J,n+1,b_3} \quad \mathbf{Z}_{M,n+1,b_3}] \in \mathbb{C}^{N_{n+1} \times 2N_{S_3}}$ . In the same representation way, the four blocks in the top left corner, in the top right corner, in the bottom left corner, and in the bottom right corner of the original  $\mathbf{Z}_{\Omega_{n+1}}$  defined by (2) can be denoted as  $\mathbf{Z}_{n,n}^{in}$ ,  $\mathbf{Z}_{n,n+1}$ ,  $\mathbf{Z}_{n+1,n}$ , and  $\mathbf{Z}_{n+1,n+1}^{out}$ , respectively. Finally, after the insertion of  $\mathbf{Z}_{\Omega_{S_3}}$  into the original  $\mathbf{Z}_{\Omega_{n+1}}$ , we continue to insert  $\mathbf{Z}_{b_3,n}$ ,  $\mathbf{Z}_{b_3,n+1}$ ,  $\mathbf{Z}_{n,b_3}$ , and

$\mathbf{Z}_{n+1,b_3}$  and come to the new submatrix

$$\mathbf{Z}_{\Omega_{n+1}}^2 = \begin{bmatrix} \mathbf{Z}_{n,n}^{in} & \mathbf{Z}_{n,b_3} & \mathbf{Z}_{n,n+1} \\ \mathbf{Z}_{b_3,n} & \mathbf{Z}_{\Omega_{S_3}} & \mathbf{Z}_{b_3,n+1} \\ \mathbf{Z}_{n+1,n} & \mathbf{Z}_{n+1,b_3} & \mathbf{Z}_{n+1,n+1}^{out} \end{bmatrix} \quad (8)$$

which has the dimensions of  $(\sum_{k=n}^{n+1} N_k + N_{S_3} + N_{b_3} + N_{i_3}) \times (2\sum_{k=n}^{n+1} N_k + 2N_{S_3} + N_{i_3})$ . Because the mutual coupling is realized only by the SIM and has no relationship with the SEM, the column numbers of  $\mathbf{Z}_{n,b_3}$  and  $\mathbf{Z}_{n+1,b_3}$  are different from that of  $\mathbf{Z}_{\Omega_{S_3}}$ . Therefore, they are aligned with  $\mathbf{Z}_{\Omega_{S_3}}$  to the left with padded zeros. Similarly,  $\mathbf{Z}_{b_3,n}$  and  $\mathbf{Z}_{b_3,n+1}$  are aligned with  $\mathbf{Z}_{\Omega_{S_3}}$  to the top with padded zeros. The aforementioned operations further increase the dimensions of  $\mathbf{Z}^1$  to  $(2\sum_{k=1}^M N_k + N_{b_1} + N_{i_1} + N_{b_2} - N_m - N_{m+1} + N_{S_3} + N_{b_3} + N_{i_3}) \times (2\sum_{k=1}^M N_k + N_{i_1} + 2N_{S_3} + N_{i_3})$  to form the new system matrix  $\mathbf{Z}^2$ . So, we synchronously increase the row number of the vector  $\mathbf{I}^1$  to  $2\sum_{k=1}^M N_k + N_{i_1} + 2N_{S_3} + N_{i_3}$ , insert the Fourier spectral coefficient vectors  $\tilde{\mathbf{H}}_{Z,b_3}$  and  $\tilde{\mathbf{E}}_{t,b_3}$  of SIM on  $S_3$  and the coefficient vector  $\mathbf{H}^{i_3}$  of the SEM nodes inside  $S_3$  into  $\mathbf{I}^1$ , and form the new coefficient vector

$$\mathbf{I}^2 = \left[ \cdots \tilde{\mathbf{H}}_{Z,m}^T \quad \tilde{\mathbf{E}}_{t,m}^T \quad (\mathbf{H}^{i_1})^T \quad \tilde{\mathbf{H}}_{Z,m+1}^T \quad \tilde{\mathbf{E}}_{t,m+1}^T \right. \\ \left. \cdots \tilde{\mathbf{H}}_{Z,n}^T \quad \tilde{\mathbf{E}}_{t,n}^T \quad \tilde{\mathbf{H}}_{Z,b_3}^T \quad \tilde{\mathbf{E}}_{t,b_3}^T \quad (\mathbf{H}^{i_3})^T \quad \tilde{\mathbf{H}}_{Z,n+1}^T \quad \tilde{\mathbf{E}}_{t,n+1}^T \cdots \right]^T. \quad (9)$$

The aforementioned process can be repeated until all the SESI matrices like (7) for all the isolated scatterers wrapped by  $S_3, \dots, S_N$  are inserted into the system matrix  $\mathbf{Z}$ . Finally, let us discuss the mutual EM coupling among the smooth surfaces  $S_3, \dots, S_N$ . Here, we just take the EM coupling between  $S_3$  and  $S_4$  as an example and assume these two scatterers are both placed in the region  $\Omega_{n+1}$ . By simultaneously taking the mutual EM coupling between  $S_3$  and the  $l_n$ th and  $l_{n+1}$ th boundaries, between  $S_4$  and the  $l_n$ th and  $l_{n+1}$ th boundaries, and between  $S_3$  and  $S_4$  into account, we reconstruct the new submatrix for the region  $\Omega_{n+1}$  as

$$\mathbf{Z}_{\Omega_{n+1}}^3 = \begin{bmatrix} \mathbf{Z}_{n,n}^{in} & \mathbf{Z}_{n,b_3} & \mathbf{Z}_{n,b_4} & \mathbf{Z}_{n,n+1} \\ \mathbf{Z}_{b_3,n} & \mathbf{Z}_{\Omega_{S_3}} & \mathbf{Z}_{b_3,b_4} & \mathbf{Z}_{b_3,n+1} \\ \mathbf{Z}_{b_4,n} & \mathbf{Z}_{b_4,b_3} & \mathbf{Z}_{\Omega_{S_4}} & \mathbf{Z}_{b_4,n+1} \\ \mathbf{Z}_{n+1,n} & \mathbf{Z}_{n+1,b_3} & \mathbf{Z}_{n+1,b_4} & \mathbf{Z}_{n+1,n+1}^{out} \end{bmatrix} \quad (10)$$

which has the dimensions of  $(\sum_{k=n}^{n+1} N_k + \sum_{k=3}^4 (N_{S_k} + N_{b_k} + N_{i_k})) \times (2\sum_{k=n}^{n+1} N_k + \sum_{k=3}^4 (2N_{S_k} + N_{i_k}))$ . We repeat the aforementioned process to assemble the final system matrix  $\mathbf{Z}^3$  which has the dimensions of  $(\sum_{k=1}^M N_k + \sum_{k=3}^N (N_{S_k} + N_{b_k} + N_{i_k}) + N_{b_1} + N_{i_1} + N_{b_2} - N_m - N_{m+1}) \times (2\sum_{k=1}^M N_k + \sum_{k=3}^N (2N_{S_k} + N_{i_k}) + N_{i_1})$ . We also repeatedly insert  $[\tilde{\mathbf{H}}_{Z,b_k}^T \quad \tilde{\mathbf{E}}_{t,b_k}^T \quad (\mathbf{H}^{i_k})^T]$  with  $k = 4, \dots, N$  to the right of  $[\tilde{\mathbf{H}}_{Z,b_3}^T \quad \tilde{\mathbf{E}}_{t,b_3}^T \quad (\mathbf{H}^{i_3})^T]$  in (9) to assemble the final vector  $\mathbf{I}^3$  whose length is  $(2\sum_{k=1}^M N_k + \sum_{k=3}^N (2N_{S_k} + N_{i_k}) + N_{i_1})$ . Meanwhile, we must increase the length of  $\mathbf{V}$  in (4) to that of  $\mathbf{I}^3$  and directly fill zero in the additional elements since the incident waves only impinge on the boundary  $l_1$ . Finally, we use the conjugate transpose of  $\mathbf{Z}^3$  to multiply two sides of the system equation like (1) and solve for the final vector  $\mathbf{I}^3$  which contains both the magnetic field coefficients inside the SEM region, e.g.,  $\mathbf{H}^{i_1}$ , and the Fourier-spectral coefficients of the tangential EM fields on the boundaries of the smooth ellipses, e.g.,  $\tilde{\mathbf{H}}_{Z,b_3}^T$  and  $\tilde{\mathbf{E}}_{t,b_3}^T$ , used to enclose the isolated inhomogeneous scatterers. The correctness of these coefficients will be validated in Section III. Furthermore, we multiply the spectral-domain radiation matrix by the vector  $\mathbf{I}^3$  to compute the scattered fields at the receiver



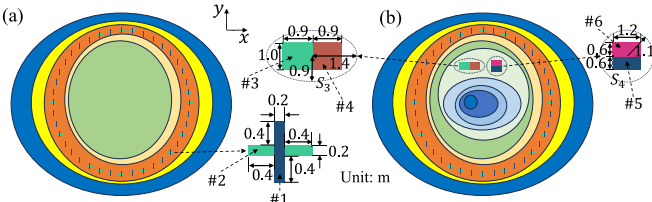


Fig. 2. Two-dimensional EM scattering models for multiple inhomogeneous objects embedded in a multilayered ellipse. (a) Forty inhomogeneous cross-shapes are embedded in the fourth layer. (b) Besides the cross-shapes, an inhomogeneous rectangle and an inhomogeneous square are also placed in the seventh layer. Geometry parameters of the embedded scatterers are annotated in the figure.

TABLE I

MODEL PARAMETERS OF THE EMBEDDED ANISOTROPIC SCATTERERS

Scatterer	Parameter	$\varepsilon_x$	$\varepsilon_y$	$\sigma_x$	$\sigma_y$	$\theta$	$\mu$
# 1 & # 5		2.1	2.6	0.2	0.3	$-\pi/6$	1.1
# 2 & # 3		2.4	2.3	0.4	0.1	$\pi/6$	1.2
# 4		4.0	3.0	0.3	0.1	$\pi/3$	1.4
# 6		3.5	3.2	0.4	0.2	$\pi/4$	1.5

Remark: the unit of  $\sigma$  is mS/m; the unit of  $\theta$  is rad.

array which also will be validated in Section III. Note the assembly of the spectral-domain radiation matrix has been discussed in [21] and will not be repeated here.

### III. NUMERICAL RESULTS

In this section, we present two numerical cases to verify the correctness and efficiency of the proposed SESI method. As shown in Fig. 2, the 2-D elliptical cylinders adopted in our models are the same as those in [21, Fig. 6]. Both their geometry and dielectric parameters are listed in [21, Table II]. In the first case as shown in Fig. 2(a), we only retain the five outermost ellipses but place 40 inhomogeneous cross-shapes between the third and fourth ellipses. The centers of these cross-shapes are located with an equal central-angle step in the circumference of a fictitious ellipse which has the center coordinate  $(-1.1, -0.75)$  m, the horizontal half-axis length 10.5 m, and the vertical half-axis length 11.0 m. In this case, we will compare the total EM fields at the centers of the 40 cross-shapes computed by our SESI method and by FEM implemented by COMSOL. We will also compare the total EM fields sampled at some representative points inside the whole computational domain by our SESI method and by FEM. For the sampling points located inside the SEM region between the third and fourth elliptical boundaries, the magnetic field values at them are evaluated by first mapping the coordinates of the sampling points in the physical domain to the coordinates in the reference domain and then substituting them into the obtained magnetic field function expanded by the second-order Gauss-Lobatto-Legendre (GLL) basis functions of SEM [26]. The electric field values at the sampling points are evaluated by performing 2-D curls to the magnetic fields which actually act on the GLL basis functions in the reference domain. Because this process is rather trivial, it will not be discussed here in detail.

In the second case as shown in Fig. 2(b), we retain all the ten ellipses. Besides the cross-shapes, in the region between the sixth and seventh ellipses, we also place an inhomogeneous rectangle and an inhomogeneous square whose centers are located at  $(-3.2, 4.5)$  and  $(1.0, 4.7)$  m, respectively. In this case, we will compare the tangential EM field values sampled on the fictitious ellipse  $S_3$  enclosing the rectangle and on the fictitious circle  $S_4$  enclosing the square and the scattered EM fields at the receiver array computed by our SESI method and by FEM. Note the geometry parameters of the embedded inhomogeneous scatterers and the fictitious boundaries are annotated

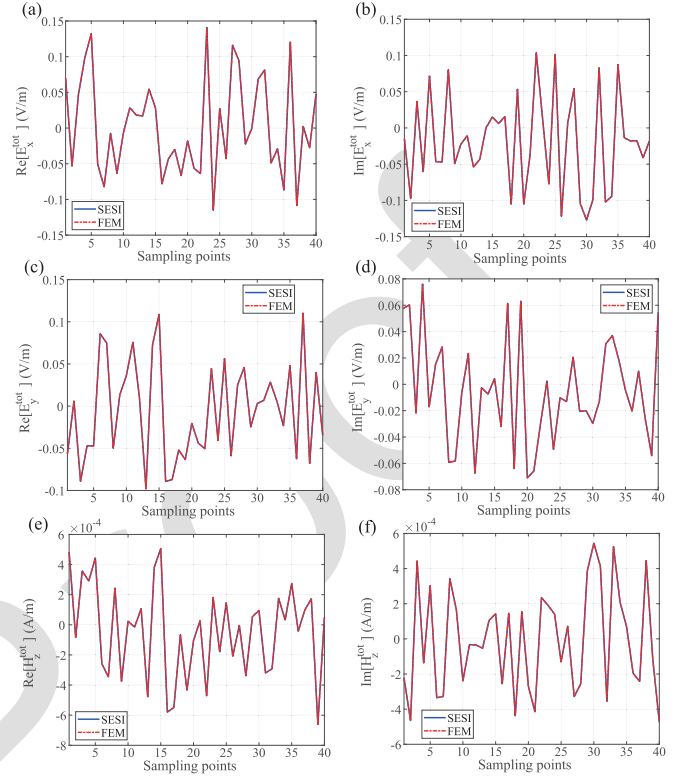


Fig. 3. Comparisons of the total EM fields at the centers of the 40 cross-shapes computed by the SESI method and FEM. (a) Real part of  $E_x^{tot}$ . (b) Imaginary part of  $E_x^{tot}$ . (c) Real part of  $E_y^{tot}$ . (d) Imaginary part of  $E_y^{tot}$ . (e) Real part of  $H_z^{tot}$ . (f) Imaginary part of  $H_z^{tot}$ .

TABLE II

MESH INFORMATION AND COMPUTATIONAL COST OF THE FIRST CASE

	mesh type	mesh number	sampling density	memory	time
FEM	triangle	10987414	25.0	255.9	857
SESI	quadrilateral	460946	31.6	20.2	256

Remark: the unit of sampling density is points per wavelength (PPW); the unit of memory is GB; the unit of time is second.

in Fig. 2. The scatterer anisotropic parameters are listed in Table I in which the permittivity and permeability are relative values. The optical-axis rotation angle  $\theta$  of the arbitrarily anisotropic scatterer is defined in [17, eq. (2)]. The configurations of magnetic dipole transmitters and the receiver array in two cases are the same as those used in [21, Sec. III]. The operation frequency is still 300 MHz. All the simulations and numerical computations are performed on a workstation with a 48-core Intel Xeon 6248R 3.0 G CPU and 1024-GB RAM. To quantify the computational error of the proposed SESI method with respect to the FEM benchmark, we define the relative error as

$$Err = \frac{\|\mathbf{f}^{SESI} - \mathbf{f}^{FEM}\|}{\|\mathbf{f}^{FEM}\|} \quad (11)$$

where  $\|\cdot\|$  denotes the  $L_2$ -norm and  $\mathbf{f}$  represents the electric field vector or the magnetic field vector in all the sampling points.

We first verify the computation accuracy and efficiency of our SESI method for evaluation of the total EM fields at the centers of the 40 arbitrarily anisotropic inhomogeneous cross-shapes and at  $7 \times 9$  sampling points inside the computational domain using the scattering model of the first case shown in Fig. 2(a). The sampling point located at the bottom left corner of the uniform  $7 \times 9$  array has the coordinate  $(-21.2, -16.0)$  m. The intervals between two adjacent sampling points in both the  $\hat{x}$ -direction and the  $\hat{y}$ -direction are 5.0 m.

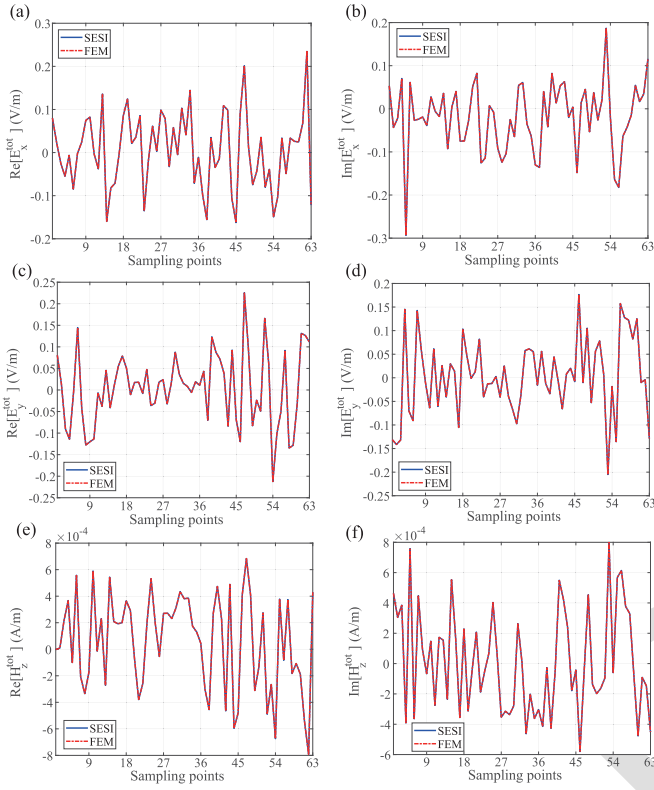


Fig. 4. Comparisons of the total EM fields at 63 typical sampling points computed by the SESI method and FEM. (a) Real part of  $E_x^{tot}$ . (b) Imaginary part of  $E_x^{tot}$ . (c) Real part of  $E_y^{tot}$ . (d) Imaginary part of  $E_y^{tot}$ . (e) Real part of  $H_z^{tot}$ . (f) Imaginary part of  $H_z^{tot}$ .

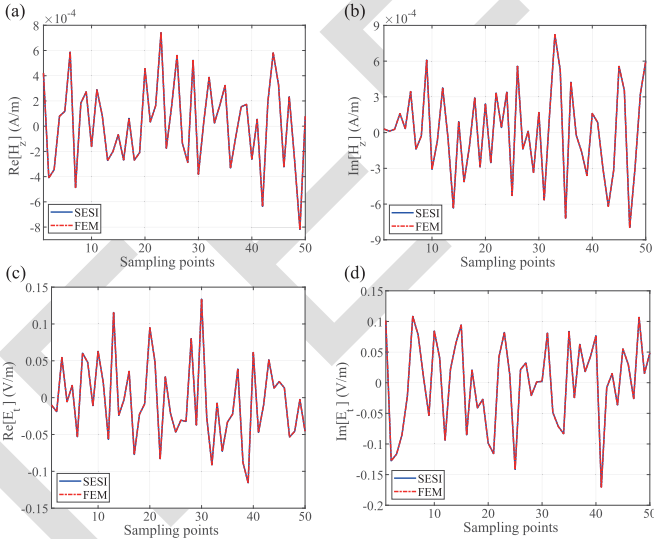


Fig. 5. Comparisons of the tangential EM fields sampled on the fictitious smooth boundaries enclosing the inhomogeneous scatterers placed between the sixth and seventh boundaries of the background elliptical cylinders computed by the SESI method and FEM. (a) Real part of  $H_z$ . (b) Imaginary part of  $H_z$ . (c) Real part of  $E_t$ . (d) Imaginary part of  $E_t$ .

The discretization mesh information for FEM and the SESI method is given in Table II.

Fig. 3 shows comparisons of the total EM fields at the 40 cross-shape centers computed by our SESI method and FEM. The relative errors of  $E_x^{tot}$ ,  $E_y^{tot}$ , and  $H_z^{tot}$  from SESI method with respect to those from FEM are 0.26%, 0.21%, and 0.03%, respectively. Fig. 4 shows comparisons of the total EM fields at the 63 sampling points computed by our SESI method and FEM. The relative errors of  $E_x^{tot}$ ,  $E_y^{tot}$ , and  $H_z^{tot}$  from SESI method with respect to those from

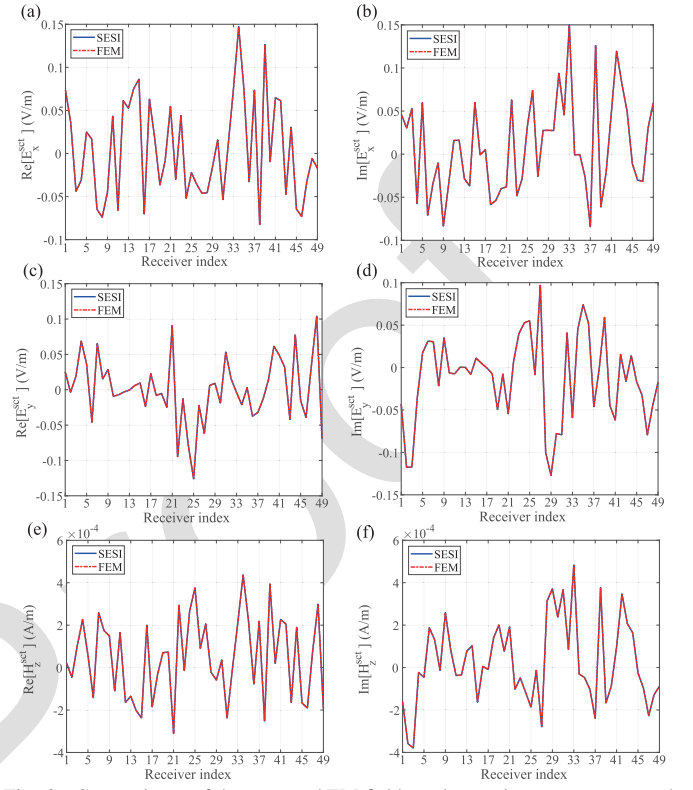


Fig. 6. Comparisons of the scattered EM fields at the receiver array computed by the SESI method and FEM. (a) Real part of  $E_x^{scat}$ . (b) Imaginary part of  $E_x^{scat}$ . (c) Real part of  $E_y^{scat}$ . (d) Imaginary part of  $E_y^{scat}$ . (e) Real part of  $H_z^{scat}$ . (f) Imaginary part of  $H_z^{scat}$ .

TABLE III

MESH INFORMATION AND COMPUTATIONAL COST OF THE SECOND CASE

	mesh type	mesh number	sampling density	memory	time
FEM	triangle	10895218	20.4	253.8	832
SESI	quadrilateral	498868	33.3	20.6	348

Remark: the unit of sampling density is PPW; the unit of memory is GB; the unit of time is second.

FEM are 0.09%, 0.07%, and 0.1%, respectively. For this case with five elliptical cylinders and 40 anisotropic embedded scatterers, the comparisons of the computational cost of FEM and the SESI method are listed in Table II. The memory refers to the peak memory in the whole computation process. Obviously, compared with the traditional FEM, the proposed SESI method can reliably compute the total EM field values no matter when the sampling points are located inside the arbitrarily anisotropic scatterers or inside the background biaxially elliptical cylinders with a much lower cost. The root reason for this big discrepancy is that FEM is implemented in the whole region enclosing the five elliptical layers while SEM is only implemented in the fourth layer in which the 40 cross-shapes are embedded.

Now let us check the computation accuracy of the tangential EM fields on the fictitious ellipse and circle enclosing inhomogeneous scatterers which are placed in the region between the sixth and seventh boundaries of the background ellipses and the scattered EM fields at the receiver array using the scattering model of the second case shown in Fig. 2(b). We pick 30 representative sampling points in the circumference of the fictitious ellipse and 20 points in the circumference of the fictitious circle for validation. These sampling points are distributed in the circumferences with equal central-angle steps. The discretization mesh information for FEM and the SESI method is given in Table III.

Fig. 5 shows comparisons of the tangential magnetic and electric fields at the 50 sampling points in the circumferences computed

by our SESI method and FEM. The relative errors of  $H_z$  and  $E_t$  from the SESI method with respect to those from FEM are 0.40% and 0.26%, respectively. Fig. 6 shows comparisons of the scattered EM fields at the receiver array computed by our SESI method and FEM. The relative errors of  $E_x^{sct}$ ,  $E_y^{sct}$ , and  $H_z^{sct}$  from SESI method with respect to those from FEM are 0.08%, 0.08%, and 0.11%, respectively. For this case with ten elliptical cylinders and multiple embedded inhomogeneous regions, the comparisons of the computational cost of FEM and the SESI method are listed in Table III. Obviously, for the evaluation of EM fields on the fictitious smooth boundaries enclosing the inhomogeneous scatterers and the scattered fields at the receiver array, the proposed SESI method also can achieve the same computation accuracy as that of FEM but with a much lower cost.

#### IV. CONCLUSION AND DISCUSSION

In this work, we extend our previous work and propose a novel hybrid SESI method to fast compute the 2-D EM scattering from multiple arbitrarily anisotropic inhomogeneous scatterers embedded in multilayered biaxially anisotropic elliptical cylinders. The new system matrix is assembled by inserting multiple SESI system submatrices into the original SIM system matrix. Meanwhile, several other submatrices are also inserted into the SIM matrix to account for the mutual EM coupling between the isolated inhomogeneous scatterers and the background elliptical boundaries as well as the mutual EM coupling among the isolated scatterers themselves. The solved vector simultaneously contains the tangential EM fields on the smooth elliptical boundaries and the magnetic field values inside the inhomogeneous regions. Several numerical experiments are implemented not only to validate the EM fields inside the inhomogeneous regions or on the fictitious boundaries enclosing the inhomogeneous regions but also to validate the scattered EM fields at the receiver array. It is found that our SESI method can achieve the same computation accuracy as the traditional FEM for EM scattering from multiple inhomogeneous scatterers embedded in multilayered elliptical cylinders but with a much lower cost. This method can be straightforwardly extended to the EM scattering scenarios with more scatterers simultaneously placed in more cylindrical regions by inserting more SESI submatrices and auxiliary matrix blocks into the original SIM system matrix.

#### REFERENCES

- [1] C. Yu et al., "Microwave imaging in layered media: 3-D image reconstruction from experimental data," *IEEE Trans. Antennas Propag.*, vol. 58, no. 2, pp. 440–448, Feb. 2010.
- [2] X. Millard and Q. Huo Liu, "Simulation of near-surface detection of objects in layered media by the BCGS-FFT method," *IEEE Trans. Geosci. Remote Sens.*, vol. 42, no. 2, pp. 327–334, Feb. 2004.
- [3] A. Abubakar, P. M. van Den Berg, and T. M. Habashy, "An integral equation approach for 2.5-dimensional forward and inverse electromagnetic scattering," *Geophys. J. Int.*, vol. 165, no. 3, pp. 744–762, Jun. 2006.
- [4] M. Dehmollaian, N. Chamanara, and C. Caloz, "Wave scattering by a cylindrical metasurface cavity of arbitrary cross section: Theory and applications," *IEEE Trans. Antennas Propag.*, vol. 67, no. 6, pp. 4059–4072, Jun. 2019.
- [5] A. Glisson and D. Wilton, "Simple and efficient numerical methods for problems of electromagnetic radiation and scattering from surfaces," *IEEE Trans. Antennas Propag.*, vol. AP-28, no. 5, pp. 593–603, Sep. 1980.
- [6] G. K. Avdikos and H. T. Anastassiou, "Computational cost estimations and comparisons for three methods of applied electromagnetics (MoM, MAS, MMAS)," *IEEE Antennas Propag. Mag.*, vol. 47, no. 1, pp. 121–129, Feb. 2005.
- [7] P. Zwamborn and P. M. van den Berg, "The three dimensional weak form of the conjugate gradient FFT method for solving scattering problems," *IEEE Trans. Microw. Theory Techn.*, vol. 40, no. 9, pp. 1757–1766, Sep. 1992.
- [8] L. Hu, L.-W. Li, and T. S. Yeo, "Analysis of scattering by large inhomogeneous bi-anisotropic objects using aim," *Prog. Electromagn. Res.*, vol. 99, pp. 21–36, 2009.
- [9] N. Engheta, W. D. Murphy, V. Rokhlin, and M. S. Vassiliou, "The fast multipole method (FMM) for electromagnetic scattering problems," *IEEE Trans. Antennas Propag.*, vol. 40, no. 6, pp. 634–641, Jun. 1992.
- [10] X.-C. Nie, L.-W. Li, N. Yuan, T. Soon Yeo, and Y.-B. Gan, "Precorrected-FFT solution of the volume integral equation for 3-D inhomogeneous dielectric objects," *IEEE Trans. Antennas Propag.*, vol. 53, no. 1, pp. 313–320, Jan. 2005.
- [11] F. Han, J. Zhuo, N. Liu, Y. Liu, H. Liu, and Q. H. Liu, "Fast solution of electromagnetic scattering for 3-D inhomogeneous anisotropic objects embedded in layered uniaxial media by the BCGS-FFT method," *IEEE Trans. Antennas Propag.*, vol. 67, no. 3, pp. 1748–1759, Mar. 2019.
- [12] R. T. Ling, "A finite-difference frequency-domain (FD-FD) approach to electromagnetic scattering problems," *J. Electromagn. Waves Appl.*, vol. 3, no. 2, pp. 107–128, Jan. 1989.
- [13] A. Taflov and K. R. Umashankar, "Review of FD-TD numerical modeling of electromagnetic wave scattering and radar cross section," *Proc. IEEE*, vol. 77, no. 5, pp. 682–699, May 1989.
- [14] W. Sun and C. A. Balanis, "Edge-based FEM solution of scattering from inhomogeneous and anisotropic objects," *IEEE Trans. Antennas Propag.*, vol. 42, no. 5, pp. 627–632, May 1994.
- [15] J.-H. Lee, T. Xiao, and Q. H. Liu, "A 3-D spectral-element method using mixed-order curl conforming vector basis functions for electromagnetic fields," *IEEE Trans. Microw. Theory Techn.*, vol. 54, no. 1, pp. 437–444, Jan. 2006.
- [16] F. Q. Hu, "A spectral boundary integral equation method for the 2D Helmholtz equation," *J. Comput. Phys.*, vol. 120, no. 2, pp. 340–347, Sep. 1995.
- [17] J. Li, Z. Li, Z. Guan, and F. Han, "2-D electromagnetic scattering and inverse scattering from anisotropic objects under TE illumination solved by the hybrid SIM/SEM," *IEEE Trans. Antennas Propag.*, vol. 72, no. 4, pp. 3517–3528, Apr. 2024.
- [18] J.-M. Jin, J. L. Volakis, and J. D. Collins, "A finite-element-boundary-integral method for scattering and radiation by two- and three-dimensional structures," *IEEE Antennas Propag. Mag.*, vol. 33, no. 3, pp. 22–32, Jun. 1991.
- [19] D. J. Hoppe, L. W. Epp, and J.-F. Lee, "A hybrid symmetric FEM/MOM formulation applied to scattering by inhomogeneous bodies of revolution," *IEEE Trans. Antennas Propag.*, vol. 42, no. 6, pp. 798–805, Jun. 1994.
- [20] E. Simsek, J. Liu, and Q. H. Liu, "A spectral integral method and hybrid SIM/FEM for layered media," *IEEE Trans. Microw. Theory Techn.*, vol. 54, no. 11, pp. 3878–3884, Nov. 2006.
- [21] Z. Guan, J. Li, and F. Han, "Exponential accuracy solutions of 2-D electromagnetic scattering from multilayered nonconcentric elliptical magnetodielectric cylinders under TE illumination," *IEEE Trans. Microw. Theory Techn.*, vol. 72, no. 5, pp. 2914–2926, May 2024.
- [22] Z. Guan, J. Liu, M. Zhuang, and Q. H. Liu, "A hybrid SESI method for electromagnetic scattering by objects in multiregion cylindrically layered media," *IEEE Trans. Microw. Theory Techn.*, vol. 69, no. 9, pp. 3967–3975, Sep. 2021.
- [23] N. Ghavami, G. Tiberi, D. J. Edwards, and A. Monorchio, "Microwave imaging through a mode-matching Bessel functions procedure," *IEEE Trans. Microw. Theory Techn.*, vol. 61, no. 8, pp. 2753–2760, Aug. 2013.
- [24] S. Karan and V. B. Ertürk, "Analysis of input impedance and mutual coupling of microstrip antennas on multilayered circular cylinders using closed-form green's function representations," *IEEE Trans. Antennas Propag.*, vol. 62, no. 11, pp. 5485–5496, Nov. 2014.
- [25] M. Nikitenko, G. B. Itskovich, and A. Seryakov, "Fast electromagnetic modeling in cylindrically layered media excited by eccentric magnetic dipole," *Radio Sci.*, vol. 51, no. 6, pp. 573–588, Jun. 2016.
- [26] C. Pozrikidis, *Introduction to Finite and Spectral Element Methods Using MATLAB*. London, U.K.: Chapman & Hall, 2014, ch. 5.